Crystal Chemical Analysis of $Nd_{9.33}Si_6O_{26}$ and $Nd_8Sr_2Si_6O_{26}$ Apatite Electrolytes using Aberration-Corrected Scanning Transmission Electron Microscopy and Impedance Spectroscopy

Tao An, [†,1] Tom Baikie, [‡] Matthew Weyland, [§] J. Felix Shin, [⊥] Peter R. Slater, [⊥] Jun Wei, [#,*] and Tim J. White [†,*]

[†] *Nanyang Technological University, School of Materials Science and Engineering, 50 Nanyang Avenue, 639798, Singapore,* [‡] *Energy Research Institute @ NTU (ERI@N), Nanyang Technological University, 1 CleanTech Loop, Singapore 637141, Singapore,* [§] *Monash Centre for Electron Microscopy and Department of Materials Engineering, Monash University, Victoria 3800, Australia,* [⊥] *School of Chemistry, University of Birmingham, Edgbaston, Birmingham, B15 2TT, UK,* and [#] *Singapore Institute of Manufacturing Technology (SIMTech), Agency for Science, Technology and Research (A*STAR), 71 Nanyang Drive, 638075, Singapore.*

KEYWORDS: solid electrolyte, apatite, scanning transmission electron microscopy, impedance spectroscopy

ABSTRACT: Lanthanoid silicate apatite solid electrolytes contain one-dimensional channels. These materials display substantial oxygen mobility at temperatures lower than conventional zirconia-based ionic conductors because interstitial oxygen displacements, mediated by *Ln* cation vacancies, have a lower activation energy. For these non-stoichiometric apatites, crystal structure solutions derived from X-ray and neutron powder diffraction yield the average atomic arrangement, but these techniques also average over local lattice disorders. Large apatite single crystals permit the evaluation of oxygen migration anisotropy using impedance spectroscopy, and the correlation of this behavior to atomic scale domain formation or defect cluster aggregation if present. Aberration-corrected scanning transmission electron microscopy, in both high angle annular dark field (HAADF) and bright field (BF) modalities, was applied to characterize the local atomic structure of $Nd_{9.33}Si_6O_{26}$ and $Nd_8Sr_2Si_6O_{26}$ apatite electrolytes. Quantitative image analysis found, the distribution of metal vacancies and dopant metal in apatites to be remarkably homogeneous at the unit cell scale. This is distinct from other oxide electrolytes including fluorites, perovskites and melilites, where domain and superstructure formation are a consequence of interstitial oxygen incorporation and prescribe the mode of ionic transport. In the present case, the unexpectedly high perfection of silicate apatites arises from the flexible topological response of one-dimensional channels penetrating the structure, which in turn, allows robust chemical tailoring of these electrolytes.

■ INTRODUCTION

Lanthanoid silicate apatites are one-dimensional tunnel structures that adopt hexagonal ($P6_3/m$) or pseudo-hexagonal crystal symmetry and are candidate electrolytes for next generation solid oxide fuel cells (SOFC) (Figure 1). These materials show significant ionic conductivity at intermediate temperatures (500-700°C)[1] that reduces mechanical stress in the cell assemblages and extends their serviceable lifetimes. The general composition of the apatite prototype is $Ln_{9.33}\square_{0.67}Si_6O_{26}$ (*Ln* = La) with Ln^{3+} vacancies (□) required for charge balance. More completely, two distinct *Ln* sites occupy the tunnel (Ln^T) and framework (Ln^F) of apatite and the formula can be recast as $[Ln^F_{3.33}\square_{0.67}][Ln^T_6][SiO_4]_6O_2$.[2] Extra-stoichiometric Ln^{3+} can be introduced with an accompanying interstitial oxygen ($2Ln^{3+} + 3O_i^{2-}$), and both atomistic modeling[3, 4] and neutron diffraction[5, 6] suggest this substitution creates an [001][7] conduction path for O^{2-}. However, intra-tunnel transport only accounts for two-thirds of the conduction, with the balance by cross-tunnel migration, which is less well understood. In any event, ionic mobility in apatites is quite distinct from the extensively studied yttria-stabilized zirconia[8] electrolytes, and other ionic conductors, such as doped-ceria[9] and La-Sr-Ga-Mg perovskites,[10] whose O^{2-} conduction is based on vacancy transport.[11]

In apatites, the dominant through-channel transport route suggested through simulation[12] was consistent with the average interstitial locations obtained by X-ray and neutron diffraction of polycrystalline[13] and single crystal[14] samples. However, microscopic observations of sufficient resolution to provide insights into defect distribution, as recently achieved for melilite-type electrolytes,[15] have been lacking. For ceramics that show sufficient stability toward high energy electrons, scanning transmission electron microscopy (STEM)[16] can reveal chemical information through atomic number (Z) or Z-contrast imaging.[17] To a first approximation, the higher the average atomic number of an atom column the greater the average scattering angle, and by collecting electrons scattered to high (>50 mrad) semi-angles with a HAADF detector high-

er average Z columns will show higher intensities. Here, we use STEM images of the neodymium silicate apatite electrolytes, $Nd_{9.33}Si_6O_{26}$ and $Nd_8Sr_2Si_6O_{26}$, to both validate the average structure and search for defective regions that may influence oxygen ion mobility. In the strontium variety, the large cation sites are fully occupied ($\square_{Ln} + 2Nd^{3+} \rightarrow 3Sr^{2+}$) with respect to $Nd_{9.33}Si_6O_{26}$ and both compositions contain a stoichiometric complement of 26 oxygen per formula unit. This apatite compositional pair was selected to most directly examine the heavy cation (Nd/Sr) distribution and correlate crystal chemistry with oxygen mobility measured by impedance spectroscopy.

■ EXPERIMENTAL METHODS

Synthesis. Single crystals of $Nd_{9.33}Si_6O_{26}$ and $Nd_8Sr_2Si_6O_{26}$ were grown using an FZ-T-4000-H-VPO-VII-PC optical floating zone furnace (Crystal Systems Corporation, Japan).[18] Polycrystalline feed rods were prepared by conventional solid state sintering. Nd_2O_3 (Alfa Aesar, 99.9%), $SrCO_3$ (99.9%, Alfa Aesar) and SiO_2 (Alfa Aesar, 99.9%) were thoroughly mixed in stoichiometric metal ratios in an agate mortar with manual grinding for 1h, followed by pre-heating (1200°C/10h) to decarbonize $SrCO_3$. The mixture was then reground for 1h to ensure homogeneity and isostatically pressed into cylindrical rods in a hydraulic press, and finally calcined (1650°C/24h) in a platinum crucible to obtain monophasic apatite feeders (7mm in diameter and 30 mm in length). The crystal growth was performed in a steady flow of Ar (2L/min) at a rate of 5mm/h to obtain clear and transparent single crystal ingots without macroscopic cracks.

Transmission Electron Microscopy. The specimens were crushed in ethanol with an agate mortar and pestle, and deposited on holey carbon films supported by copper grids. The microscopy was performed with an FEI Titan^3 field emission gun (FEG) transmission electron microscope fitted with aberration-correctors on both the illumination and imaging system and operated at 300 kV. Alignment and correction of the C_s-corrector allowed images to be collected at a probe convergence semi-angle of 15.1 mrad, corresponding to an aperture limited probe size of ~1.2Å. The inner collection semi-angle of the HAADF detector was 57 mrad and outer collection angle for the BF detector was 14 mrad. CRISP[19] software was used for the processing of the experimental images by performing fast Fourier transformation (FFT) over a selected area of ~100 unit cells to generate the diffraction pattern, which was then converted back to high resolution images via inverse FFT and the signal-to-noise ratio was thus greatly improved. HAADF images and position averaged convergent beam electron diffraction (PACBED)[20] patterns were also simulated with JEMS,[21] using the CIF from X-ray diffraction and the microscope parameters specified above. ImageJ[22] was used to obtain the line profiles across the atomic columns centers to quantitatively assess the relative contrast in the experimental and simulated images.

Impedance Spectroscopy. Conductivity measurements were carried out in air from 200°C to 860°C using AC impedance spectroscopy (Hewlett Packard 4192A impedance analyzer, frequency range 10 Hz to 13 MHz, applied voltage of 0.1V). Specimen discs of ~5mm diameter and 2-3mm thickness were cut perpendicularly from the as-grown crystals, and the crystallographic orientation was confirmed with electron backscatter diffraction (ESBD) as described elsewhere.[18] Gold paste was applied to opposing disc surfaces and thermally bonded (700°C/1h). The spectra were analyzed with ZView software,[23] which estimates the resistance and capacitance associated with the equivalent circuits through complex nonlinear least squares fitting; the equivalent circuit is as described previously,[24] and is typical for solid oxide ion conductors.[25] As noted in our previous study discussing the conductivities of $Nd_{9.33}Si_6O_{26}$ and Al-doped analogues, the circuit consists of a "bulk" component and a second component arranged in series, with each component including a resistor and constant-phase element (CPE) connected in parallel. The capacitance of the second component semicircle was of the order of 10^{-7} F·cm^{-1}, which is larger than the typical value for a grain boundary response and may be correlated with a surface/interface layer effect[24]. The conductivity values reported are based on the first semicircle (bulk) component, with representative fits presented in details elsewhere[24].

■ RESULTS AND DISCUSSION

The [001] projection of apatite separates the two types of Nd (Nd^T and Nd^F) atomic columns. The scattering power of the Nd^F and Nd^T columns are distinct, as the former resides in the 4*f* Wyckoff position where two Nd reside in each column per unit cell, while the latter occupies the 6*h* site, leading to a single atom per column per unit cell. Therefore, the Nd^F atomic columns nominally scatter electrons twice as effectively as Nd^T (ignoring for now the influence of vacancies) to yield distinct HAADF contrast. For both $Nd_{9.33}Si_6O_{26}$ and $Nd_8Sr_2Si_6O_{26}$, the scattering from Si (Z=14) and O (Z=8) is relatively minor in a matrix dominated by Nd (Z=60) and Sr (Z=38). The presence of vacancies or substitution of Sr in the Nd^F sites reduces electron scattering and the HAADF signal. While in some situations it is possible to link composition directly to the collected STEM signal,[26, 27] the difficulty in obtaining reliable thickness measurements makes an *ab-initio* assessment of contrast impractical. However, the relative contrast can be examined with the aid of image simulation, and the frequency, nature and distribution of chemical defects established.

Single crystal determinations of the $Nd_{9.33}Si_6O_{26}$ and $Nd_8Sr_2Si_6O_{26}$ apatite structures using X-rays and neutrons[5] conformed to $P6_3/m$ (see supplementary Table S1), and were used as input to calculate HAADF images. For $Nd_8Sr_2Si_6O_{26}$, the inclusion of larger Sr^{2+} (IR = 1.18Å)[28] in place of Nd^{3+} (0.983Å)[28] causes the unit cell to dilate, particularly in the *c* axis direction, but with a slight contraction in the basal plane. This is expected since apatite is especially flexible in (001) through adjustment of the Nd^FO_6 metaprism twist angle;[29] the increase from 22.4_3° (in $Nd_{9.33}Si_6O_{26}$) to 25.1_7° ($Nd_8Sr_2Si_6O_{26}$) confirms the distinct preference of Sr^{2+} for the Nd^F site that causes framework expansion with a concomitant reduction of the tunnel diameter. However, X-ray diffraction cannot establish unambiguously the partitioning of Sr over the Nd^F and Nd^T sites as both site vacancies and Sr reduce scattering; a parallel neutron study has revealed the incorporation of Sr to be wholly on the framework site.[5] Consequently, for X-ray analysis Sr is constrained to be fully tenanted at Nd^F. Using the contrast criteria described in the previous paragraph, HAADF imaging provided direct confirmation that Sr resides in the framework (Nd^F) (Figure 2), and moreover, shows the distribution of the alkaline earth to be homogeneous; in other words, the proportion of Sr/Nd in adjacent framework cation columns was not detectably variable. Neutron diffraction found the principal difference between the Sr-free and Sr-

bearing apatites was the splitting of the O(3) site (12*i*) in the former. Such degeneracy is sometimes indicative of domain or superstructure formation, but the HAADF experiments found crystals with imperceptible heterogeneity amongst the Nd^F and Nd^T columns and an absence of domain mosaics.

Thickness measurements were collected from PACBED patterns that over a range of thickness were compared with simulations (Figure 3a), and the good match between the experimental and the simulated at 44 nm (Figure 3b) suggests the $Nd_{9.33}Si_6O_{26}$ specimen thickness to be about 63 unit cells. However, the $Nd_8Sr_2Si_6O_{26}$ specimen is found to have a much less thickness of 2 nm, which is equivalent to 3 unit cells (Figure 3c). This analysis will be affected by small crystal misalignments relative to the electron beam, variations in thickness across the field of view and deposition of surface oxide during observation. With the thickness of the specimens determined, the HAADF images can be simulated accordingly and compared with the experimental ones, and their quantitative analysis can probe the vacancy concentration at Nd^F for $Nd_{9.33}Si_6O_{26}$ (Figure 4a) as well as the Nd/Sr partition among Nd^F and Nd^T sites in $Nd_8Sr_2Si_6O_{26}$ (Figure 4b) by plotting the line profiles across the Nd^F and Nd^T scattering centers. For undoped $Nd_{9.33}Si_6O_{26}$, it was found that the contrast ratio between Nd^F and Nd^T (1.63:1) of the experimental image agrees with the ideal (1.60:1), based on 13.3%-13.6% Nd^F site vacancy as determined from single crystal X-ray and neutron diffraction.[5] For $Nd_8Sr_2Si_6O_{26}$, HAADF simulations were carried out for three discrete models – Sr solely in the framework $[Nd_2Sr_2]^F[Nd_6]^TSi_6O_{26}$; Sr evenly spread in $[Nd_3Sr]^F[Nd_5Sr]^TSi_6O_{26}$; and Sr resident in the tunnel $[Nd_4]^F[Nd_4Sr_2]^TSi_6O_{26}$. The superior agreement with the first model is evident and consistent with the X-ray and neutron data,[5] with the contrast ratio between Nd^F/Sr and Nd^T centers of the experimental image (1.36:1) matching the simulated (1.37:1). From the HAADF experiments, the homogeneous distribution of Ln^F vacancies and Sr^F dopant implies the interstitial oxygen should be evenly dispersed through the apatite crystals. This was confirmed by BF imaging of $Nd_8Sr_2Si_6O_{26}$ (Figure 5), where the bright contrast shows the SiO_4 groups and the tunnel O(4). Thus, these thin crystal sections are chemically homogenous.

The ionic conductivities of $Nd_{9.33}Si_6O_{26}$ and $Nd_8Sr_2Si_6O_{26}$ along *c* are invariably higher than in the *ab* basal plane, although for the latter, where cation vacancies are eliminated by Sr-doping, intratunnel ionic conductivity is an order-of-magnitude lower than intertunnel mobility (Figure 6). However, the difference between conductivity along [001] and [100] for $Nd_8Sr_2Si_6O_{26}$ is less anisotropic, an effect previously observed in aluminum-doped $Nd_{9.33+x/3}Al_xSi_{6-x}O_{26}$.[24] The linearity of the conduction plots indicate constant activation energy over the measured temperature range, with the only exception being the conductivity of undoped $Nd_{9.33}Si_6O_{26}$ along *c* axis, which shows a negative inflection at ~500°C, caused by the change in migration path of the interstitial oxygen. This may indicate a degree of interstitial defect trapping at low temperatures, as shown for apatite germanates.[30] The absence of cation vacancies in $Nd_8Sr_2Si_6O_{26}$ ensures the framework more rigid, temperature dependent dimorphism or trimorphism is eliminated,[31, 32] and consequently [001] conductivity does not show a change in activation energy.

■ CONCLUSION

In summary, atomic-scale *Z*-contrast images permit differentiation of Nd, Sr and the lighter elements (Si and O). By correlating electron scattering with the structure models from single crystal X-ray and neutron diffraction, the presence of cation vacancies and the incorporation of Sr at the Nd^F site have been confirmed. These apatite electrolytes are exceptionally chemically and topologically homogeneous when compared to other classes of oxide electrolytes. Impedance measurements revealed the essential role of Nd vacancies that enhance [001] conductivity by two orders of magnitude. As the primary conduction mechanism in apatites is based on interstitial transport, it is favorable to have a higher symmetry ($P6_3/m$) with minimal structural distortion for optimal performance. This is quite different to other ionic conductors, such as melilites and perovskites, which benefit from structural defects and modulations that accommodate interstitial oxygen, and provide the structural adaptability required to enhance mobility.[33] STEM is an invaluable tool to directly monitor the dopant distributions and structural defects in electrolytes, and can be used to validate and optimize the design of SOFC apatite ion conductors. The present investigation provides the first quantitative analysis of the nanostructure of pristine apatite electrolytes and creates a baseline for evaluating defect evolution after exposure to high temperature environments. Future studies will investigate silicate apatites after extended deployment in fuel cells to establish their chemical stability, defect distribution, and identify possible changes in the oxygen migration mechanism.

ASSOCIATED CONTENT

Supporting Information Available: Original HAADF images of $Nd_{9.33}Si_6O_{26}$ and $Nd_8Sr_2Si_6O_{26}$, their atomic positions and anisotropic displacement parameters (PDF); single crystal X-ray diffraction data (CIF); and structure factors (ASCII). This material is available free of charge via the Internet at http://pubs.acs.org.

AUTHOR INFORMATION

Corresponding Author

*E-mail: jwei@simtech.a-star.edu.sg; tjwhite@ntu.edu.sg.

Present Addresses

[1]Present address: Institute of Materials Research and Engineering (IMRE), Agency for Science, Technology and Research (A*STAR), 3 Research Link, Singapore 117602, Singapore.

Notes

The authors declare no competing financial interest.

ACKNOWLEDGMENT

We would like to acknowledge the Agency for Science, Technology and Research (A*STAR) PSF grant 082 101 0021 'Optimization of Oxygen Sublattices in Solid Oxide Fuel Cell Apatite Electrolytes' for funding the work and Ministry of Education (MOE) Tier 2 grant T208B1212 for enabling the purchase of a single crystal X-ray diffractometer. The authors acknowledge use of facilities within the Monash Centre for Electron Microscopy. This Titan instrument was part funded by the Australian Research Council grant LE0454166.

REFERENCES

1. Nakayama, S.; Kagayama, T.; Aono, H.; Sadoaka, Y., Ionic conductivity of lanthanoid silicates, $Ln_{10}(SiO_4)_6O_3$ (*Ln* = La, Nd, Sm,

Gd, Dy, Y, Ho, Er and Yb). *J. Mater. Chem.* **1995,** 5, (11), 1801-1806.

2. Pramana, S. S.; Klooster, W. T.; White, T. J., A taxonomy of apatite frameworks for the crystal chemical design of fuel cell electrolytes. *J. Solid State Chem.* **2008,** 181, 1717-1722.

3. Béchade, E.; Masson, O.; Iwata, T.; Julien, I.; Fukuda, K.; Thomas, P.; Champion, E., Diffusion Path and Conduction Mechanism of Oxide Ions in Apatite-Type Lanthanum Silicates. *Chem. Mater.* **2009,** 21, (12), 2508-2517.

4. Matsunaga, K.; Toyoura, K., First-principles analysis of oxide-ion conduction mechanism in lanthanum silicate. *J. Mater. Chem.* **2012,** 22, (15), 7265-7273.

5. An, T.; Orera, A.; Baikie, T.; Herrin, J. S.; Piltz, R. O.; Slater, P. R.; White, T. J.; Sanjuán, M. L., Structural Study of the Apatite $Nd_8Sr_2Si_6O_{26}$ by Laue Neutron Diffraction and Single-Crystal Raman Spectroscopy. *Inorg. Chem.* **2014,** 53, (17), 9416–9423.

6. Ali, R.; Yashima, M.; Matsushita, Y.; Yoshioka, H.; Ohoyama, K.; Izumi, F., Diffusion Path of Oxide Ions in an Apatite-Type Ionic Conductor $La_{9.69}(Si_{5.70}Mg_{0.30})O_{26.24}$. *Chem. Mater.* **2008,** 20, (16), 5203-5208.

7. Tolchard, J. R.; Islam, M. S.; Slater, P. R., Defect chemistry and oxygen ion migration in the apatite-type materials $La_{9.33}Si_6O_{26}$ and $La_8Sr_2Si_6O_{26}$. *J. Mater. Chem.* **2003,** 13, (8), 1956-1961.

8. Mori, M.; Abe, T.; Itoh, H.; Yamamoto, O.; Takeda, Y.; Kawahara, T., Cubic-stabilized zirconia and alumina composites as electrolytes in planar type solid oxide fuel cells. *Solid State Ionics* **1994,** 74, (3–4), 157-164.

9. Inaba, H.; Tagawa, H., Ceria-based solid electrolytes. *Solid State Ionics* **1996,** 83, (1-2), 1-16.

10. Ishihara, T.; Matsuda, H.; Takita, Y., Doped $LaGaO_3$ Perovskite Type Oxide as a New Oxide Ionic Conductor. *J. Am. Chem. Soc.* **1994,** 116, (9), 3801-3803.

11. Kharton, V. V.; Marques, F. M. B.; Atkinson, A., Transport properties of solid oxide electrolyte ceramics: a brief review. *Solid State Ionics* **2004,** 174, (1-4), 135-149.

12. Jones, A.; Slater, P. R.; Islam, M. S., Local defect structures and ion transport mechanisms in the oxygen-excess apatite $La_{9.67}(SiO_4)_6O_{2.5}$. *Chem. Mater.* **2008,** 20, 5055-5060.

13. Iwata, T.; Fukuda, K.; Béchade, E.; Masson, O.; Julien, I.; Champion, E.; Thomas, P., Structural change of oxide-ion-conducting lanthanum silicate on heating from 295 to 1073 K. *Solid State Ionics* **2007,** 178, (27–28), 1523-1529.

14. Okudera, H.; Masubuchi, Y.; Kikkawa, S.; Yoshiasa, A., Structure of oxide ion-conducting lanthanum oxyapatite, $La_{9.33}(SiO_4)_6O_2$. *Solid State Ionics* **2005,** 176, (15–16), 1473-1478.

15. Wei, F.; Williams, T.; An, T.; Baikie, T.; Kloc, C.; Wei, J.; White, T., Observation of atomic scale compositional and displacive modulations in incommensurate melilite electrolytes. *J. Solid State Chem.* **2013,** 203, (0), 291-296.

16. Krivanek, O. L.; Chisholm, M. F.; Murfitt, M. F.; Dellby, N., Scanning transmission electron microscopy: Albert Crewe's vision and beyond. *Ultramicroscopy* **2012,** 123, (0), 90-98.

17. Pennycook, S. J.; Jesson, D. E., High-resolution Z-contrast imaging of crystals. *Ultramicroscopy* **1991,** 37, (1–4), 14-38.

18. An, T.; Baikie, T.; Wei, F.; Li, H.; Brink, F.; Wei, J.; Ngoh, S. L.; White, T. J.; Kloc, C., Single crystal growth of apatite-type Al-doped neodymium silicates by the floating zone method. *J. Cryst. Growth* **2011,** 333, (1), 70-73.

19. Hovmöller, S., CRISP: crystallographic image processing on a personal computer. *Ultramicroscopy* **1992,** 41, 121-135.

20. LeBeau, J. M.; Findlay, S. D.; Allen, L. J.; Stemmer, S., Position averaged convergent beam electron diffraction: Theory and applications. *Ultramicroscopy* **2010,** 110, (2), 118-125.

21. Stadelmann, P. *Electron Microscopy Software Java Version*, 3.6907U2011; 12M-EPFL, CH-1015, Switzerland, 2011.

22. Schneider, C. A.; Rasband, W. S.; Eliceiri, K. W., NIH Image to ImageJ: 25 years of image analysis. *Nature Methods* **2012,** 9, (7), 671-675.

23. Johnson, D. *ZView: a Software Program for IES Analysis*, 3.1c; Scribner Associates Inc.: Southern Pines, NC, 2007.

24. An, T.; Baikie, T.; Wei, F.; Pramana, S. S.; Schreyer, M. K.; Piltz, R. O.; Shin, J. F.; Wei, J.; Slater, P. R.; White, T. J., Crystallographic Correlations with Anisotropic Oxide Ion Conduction in Aluminum-Doped Neodymium Silicate Apatite Electrolytes. *Chem. Mater.* **2013,** 25, (7), 1109-1120.

25. Abram, E. J.; Sinclair, D. C.; West, A. R., A Strategy for Analysis and Modelling of Impedance Spectroscopy Data of Electroceramics: Doped Lanthanum Gallate. *J. Electroceram.* **2003,** 10, (3), 165-177.

26. Dwyer, C.; Maunders, C.; Zheng, C. L.; Weyland, M.; Tiemeijer, P. C.; Etheridge, J., Sub-0.1 nm-resolution quantitative scanning transmission electron microscopy without adjustable parameters. *Appl. Phys. Lett.* **2012,** 100, (19), 191915-4.

27. LeBeau, J. M.; Findlay, S. D.; Allen, L. J.; Stemmer, S., Standardless Atom Counting in Scanning Transmission Electron Microscopy. *Nano Lett.* **2010,** 10, (11), 4405-4408.

28. Shannon, R. D., Revised Effective Ionic Radii and Systematic Studies of Interatomic Distances in Halides and Chalcogenides. *Acta Crystallogr. Sect. A* **1976,** 32, 751-767.

29. Lim, S. C.; Baikie, T.; Pramana, S. S.; Smith, R.; White, T. J., Apatite metaprism twist angle (φ) as a tool for crystallochemical diagnosis. *J. Solid State Chem.* **2011,** 184, (11), 2978-2986.

30. Orera, A.; Sanjuán, M. L.; Kendrick, E.; Orera, V. M.; Slater, P. R., Raman spectroscopy studies of apatite-type germanate oxide ion conductors: correlation with interstitial oxide ion location and conduction. *J. Mater. Chem.* **2010,** 20, 2170-2175.

31. Pramana, S. S.; White, T. J.; Schreyer, M. K.; Ferraris, C.; Slater, P. R.; Orera, A.; Bastow, T. J.; Mangold, S.; Doyle, S.; Liu, T.; Fajar, A.; Srinivasan, M.; Baikie, T., Pseudomorphic 2A→ ₂M→ ₂H phase transitions in lanthanum strontium germanate electrolyte apatites. *Dalton Trans.* **2009**, (39), 8280-8291.

32. Pramana, S. S.; Baikie, T.; Kendrick, E.; Schreyer, M. K.; Slater, P. R.; White, T. J., Crystal chemistry and optimization of conductivity in 2A, 2M and 2H alkaline earth lanthanum germanate oxyapatites electrolyte polytypes. *Solid State Ionics* **2010,** 181, (25-26), 1189-1196.

33. Wei, F.; Baikie, T.; An, T.; Schreyer, M.; Kloc, C.; White, T. J., Five-Dimensional Incommensurate Structure of the Melilite Electrolyte $[CaNd]_2[Ga]_2[Ga2O7]_2$. *J. Am. Chem. Soc.* **2011,** 133, (38), 15200-15211.

34. Okudera, H.; Yoshiasa, A.; Masubuchi, Y.; Higuchi, M.; Kikkawa, S., Determinations of crystallographic space group and atomic arrangements in oxide-ion-conducting $Nd_{9.33}(SiO_4)_6O_2$. *Z. Kristallogr.* **2004,** 219, (1-2004), 27-31.

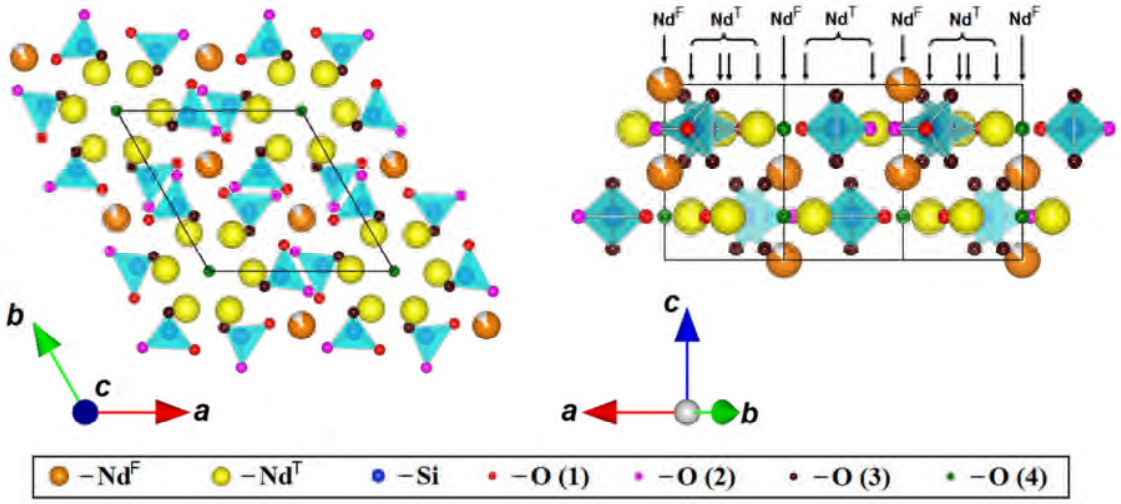

Figure 1. Polyhedral and atomic column representation of $Nd_{9.33}Si_6O_{26}$ with vacancies reporting to the framework Nd^F site[34] (illustrated by the filled area of the sphere). The Nd^F atoms are located near the centers of NdO_6 metaprisms that are corner-connected to rigid SiO_4 groups, forming a framework enclosing the tunnel Nd^T atoms and the pair of O(4) located along the *c* axis. For $P6_3/m$ the structural formula can be expressed as $[Nd^F{}_{3.33}\square_{0.67}][Nd^T{}_6][SiO_4]_6O_2$.

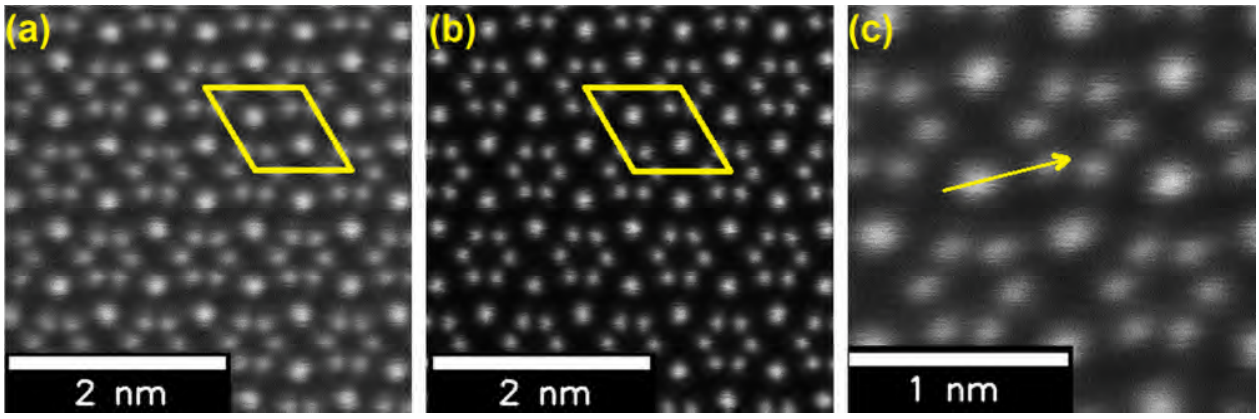

Figure 2. [001] HAADF images of (a) $Nd_{9.33}Si_6O_{26}$ and (b) $Nd_8Sr_2Si_6O_{26}$. Such images, collected from much larger regions (see supplementary information (Figures S1 and S2)), show little contrast variation. (c) The positioning of the line scan used for quantitative analysis in Figure 4 crosses the Nd^F (left side) and Nd^T (right side) atomic columns.

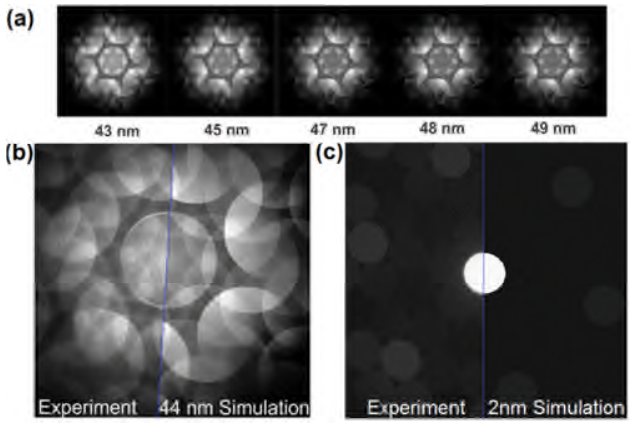

Figure 3. The determination of thickness of specimens from which the HAADF images in Figure 2 were collected. (a) PACBED patterns of $Nd_{9.33}Si_6O_{26}$ were simulated over a range of thickness and compared with (b) the original experimental PACBED pattern collected at 2.8 mrad convergence angle, and its good match with the simulated PACBED pattern at 44 nm suggests the $Nd_{9.33}Si_6O_{26}$ specimen to have a thickness of 63 unit cells (c = 0.7016 nm). (c) The good match between the experimental PACBED pattern collected at 1.2 mrad convergence angle and the simulated pattern at 2 nm thickness suggests the $Nd_8Sr_2Si_6O_{26}$ specimen to have a much less thickness of 3 unit cells (c = 0.7102).

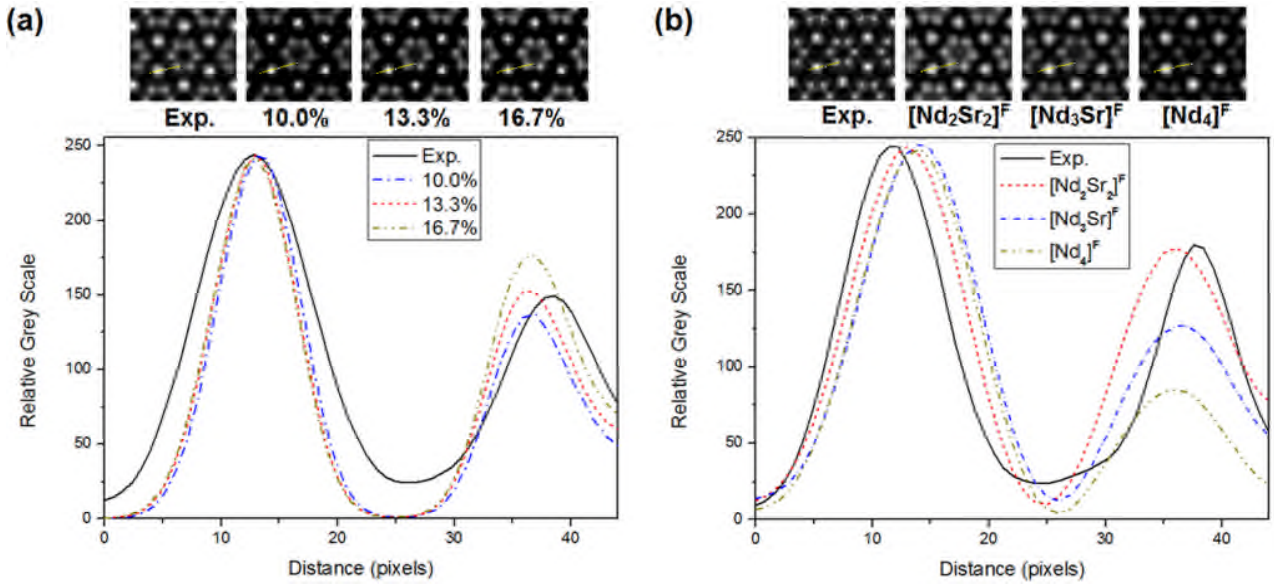

Figure 4. Quantitative comparison of $[Ln]^F$-$[Ln]^T$ line scan intensities of (a) an experimental $Nd_{9.33}Si_6O_{26}$ HAADF image (1.63:1) with simulated images calculated using single crystal X-ray diffraction data (with 13.3% vacancy at Nd^F) (1.60:1) and calculation of modified chemistries containing 10.0% (1.77:1) and 16.7% (1.37:1) vacancies at the Nd^F site; and (b) an experimental HAADF image of $Nd_8Sr_2Si_6O_{26}$ (1.36:1) compared with the simulated intensity of three models: $[Nd_2Sr_2]^F[Nd_6]^TSi_6O_{26}$ (Sr solely doped at Nd^F) (1.37:1), $[Nd_3Sr]^F[Nd_5Sr]^TSi_6O_{26}$ (Sr is evenly doped at Nd^F and Nd^T) (1.94:1) and $[Nd_4]^F[Nd_4Sr_2]^TSi_6O_{26}$ (Sr is solely doped at Nd^T) (2.86:1). For $Nd_{9.33}Si_6O_{26}$, the presence of vacancies at Nd^F is also confirmed by quantitative comparison of the line scan intensities between experimental image and that of a hypothetical case without vacancy at Nd^F site (see Figure S3 in the supplementary information). As Sr is significantly lighter than Nd, its doping leads to a decrease in the brightness of the corresponding atomic column contrast, and validates the complete partitioning of Sr to the framework position as suggested by X-ray and neutron diffraction.

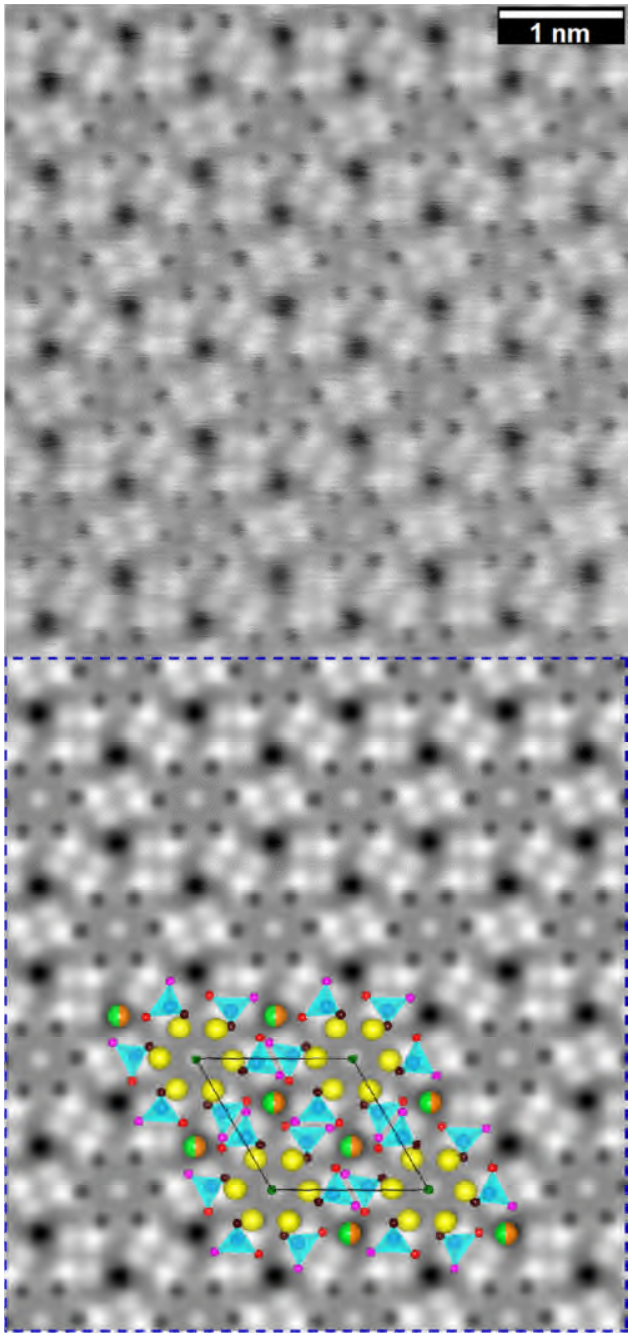

Figure 5. The BF STEM image of $Nd_8Sr_2Si_6O_{26}$ allows direct observation of SiO_4 tetrahedra and tunnel O(4) and confirms the expected homogeneity of light atom distribution inferred from the HAADF micrographs (Figure 4). Bottommost is the processed image with CRISP software[19] where *P*6 plane symmetry is imposed.

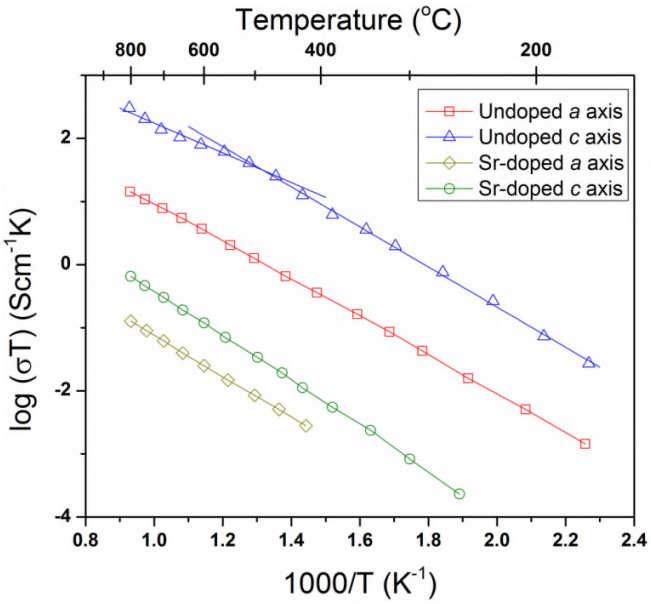

Figure 6. An Arrhenius plot of $Nd_{9.33}Si_6O_{26}$ (undoped) and $Nd_8Sr_2Si_6O_{26}$ (Sr-doped) ionic conductivity (σ) yields an activation energy (E_a) of ≈0.59-0.71eV. The conductivity are measured along both [001] (i.e. the *c* axis direction) and perpendicular to [001] (i.e. across the *ab* basal plane). The inflection in the *c*-axis conduction for $Nd_{9.33}Si_6O_{26}$ is indicative of a change in activation energy, and reflecting a degree of defect trapping at low temperatures.

Scanning transmission electron microscopy (STEM) images with atomic-scale resolution are correlated with crystallographic structure established by single crystal X-ray diffraction.